

Automated Anatomical Likelihood Driven Extraction and Branching Detection of Aortic Arch in 3-D Chest CT

Marco Feuerstein¹, Takayuki Kitasaka^{2,3}, Kensaku Mori^{1,3}

¹ Graduate School of Information Science, Nagoya University, Japan,
fmarco@suenaga.m.is.nagoya-u.ac.jp,

² Faculty of Information Science, Aichi Institute of Technology, Japan,

³ MEXT Innovation Center for Preventive Medical Engineering, Nagoya University,
Japan.

Abstract. The extraction and analysis of the aortic arch in chest computed tomography (CT) data can be an important preliminary step for the diagnosis and treatment planning of e.g. lung cancer. We here present a new method for automatic aortic arch extraction and detection of the main arterial branchings that may serve as segmentation seeds or as landmarks for intra- and interpatient registration of the mediastinum. Our method, which is based on Hough and Euclidean distance transforms and probability weighting, works on both contrast enhanced and non-contrast CT. A comparison to data manually extracted from 40 cases shows its robustness at an acceptable overall runtime.

1 Introduction

The automatic extraction of the aortic arch in computed tomography (CT) data of the chest has gained in importance in recent years, in particular to reduce the work load of physicians during diagnosis and treatment planning. As the aorta is the major vessel in the mediastinum, its automatic segmentation can be a first step for various tasks such as the definition of other mediastinal anatomy or lymph node stations for lung cancer staging. A delineation of the mediastinal vasculature for instance can be important for planning of transbronchial needle aspiration to estimate the optimal path of biopsy needles avoiding collisions with vasculature [1].

Moreover, when comparing several arches of the aorta across different data sets of the same patient or across different patients, their precise and accurate alignment is desirable to compare similarities or variances. An intuitive way to perform such a registration is to first align their arterial branchings and then refine this initial alignment towards the ascending and descending aorta.

However, the determination of the aortic arch and its branchings in CT images is not trivial, as the aortic arch frequently merges with adjacent tissue of the same image intensity, making an automation more difficult. Furthermore, only about 94.3% of all patients show a typical branching pattern, i.e. innominate, left common carotid, and left subclavian arteries, in that order [2].

The purpose of this work is two-fold. First, we present a method for fully automatic aortic arch segmentation, which works robust on both contrast enhanced and non-contrast chest CT and extends previously presented methods. Second, we utilize the segmentation result in a new algorithm to automatically determine the branchings of the aorta. These branchings can be utilized e.g. for intra- and interpatient registration of the mediastinum or as seed points for a subsequent segmentation of the branches.

Several research groups proposed methods for the extraction of the aorta in contrast enhanced data. For example, various semi-automatic and interactive methods were presented for the extraction of the abdominal aorta lumen in CT angiography data [3–5]. Behrens et al. [6] presented an approach to extract tubular structures using randomized Hough transform and Kalman filtering. It requires a starting point, a coarse direction, and an approximate radius, and was tested on the aortic arch in magnetic resonance imaging angiography data. Kovács et al. [7] utilize the Hough transform to initialize an extraction of the aortic arch in contrast enhanced CT based on a deformable surface model. O’Donnell et al. [8] and Peters et al. [9] also proposed a deformable model to fit the aorta in CT angiography data. While the former [8] was only tested on one data set, the latter [9] showed segmentation errors for lower contrast. Low contrast is a common issue for all methods developed for contrast enhanced data.

In non-contrast CT, the Hough transform was also utilized by a few groups, e.g. by Išgum et al. [10] and Kurkure et al. [11] to detect the ascending and descending part of the thoracic aorta, but not its arch or branchings. Kitasaka et al. [12] were the first to fit an aorta model to non-contrast chest CT. However, as their method only includes one model, it cannot cover a large range of variations of the aortic shape. Taeprasartsit and Higgins [13] therefore extended this approach to three models and to work on both non-contrast and contrast enhanced data. After manually selecting the carina tracheae, it could successfully extract the aorta for 12 test cases. For one case, no appropriate model could be selected.

To our knowledge, there has been no prior work on the automatic extraction of the main branchings of the aortic arch.

2 Method

Based on general a priori knowledge of the mediastinal anatomy, our method first performs a series of circular Hough transforms to delineate the aortic arch and its centerline. Using a B-spline to represent this centerline, the B-spline is then fitted to a likelihood image, which basically consists of Euclidean distances to possible aorta edges. After successful centerline fitting, the Euclidean distances along the centerline are used to recover the full segmentation of the aortic arch.

We eventually determine the main arterial branchings in a parallel projection image of the segmentation and likelihood image of the aortic arch (in superior direction) by weighing up three factors influencing the probability of branching candidates: vessel thickness (represented by the likelihood image), proximity to the projected centerline, and relative branching positions.

2.1 Preprocessing

Before any further processing, we smooth the input data by a 3-D median filter of size s_m (see Table 1 for all subsequent variables) to reduce image noise. Moreover, we assume the patient to be placed in true supine position, as this is the case for most chest CT acquisitions. However, if the patient is positioned differently, we could identify representative and unique anatomic landmarks such as bones [14], perform a principal component analysis or the like to estimate the main body axes, and rotate the data set accordingly.

The lung (enclosing the mediastinum) and the carina tracheae (within the mediastinum) are important anatomical landmarks, which we here utilize to estimate the first centerline points of the aorta. We automatically determine a rough segmentation of the lung area and its bounding box applying an approach similar to [15]. Within the bounding box of the lung, we search for the position of the carina by extracting the airway tree [16] and checking subsequent axial slices for the ridge between the openings of the right and left main bronchi.⁴

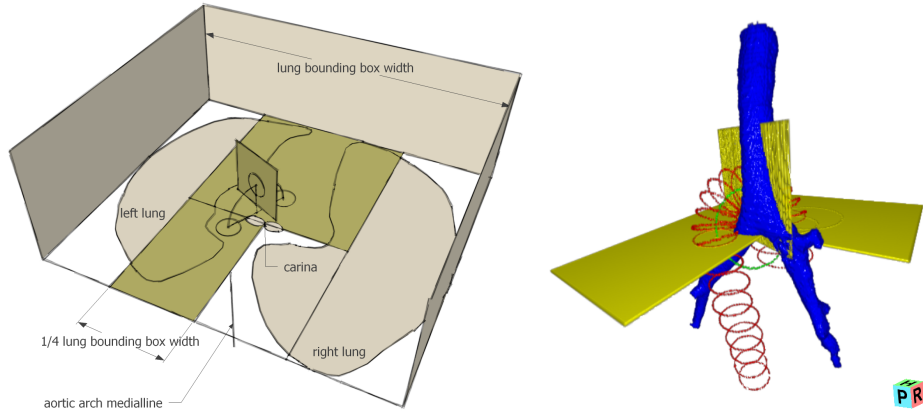
We furthermore approximate a maximum mediastinal bounding box, which is centered at the position of the carina on the mediolateral axis and at the center of the lung bounding box on the anteroposterior and superior-inferior axes. It has half the diameter (width) of the lung bounding box along the mediolateral axis and the full diameter of the lung bounding box along the anteroposterior and superior-inferior axes (cf. Fig. 1a).

2.2 Aortic Arch Segmentation

Our aortic arch segmentation method is an enhancement of the works of [7, 12, 13]. As in [12, 13], high gradients of a CT image are extracted (representing approximate blood vessel edges) and a Euclidean distance transform is applied to the gradient image to obtain the likelihood of each voxel being closer or further away from the centerline of the aorta. In [12, 13] this is followed by fitting a predetermined model of the aortic arch centerline to this likelihood image. However, to be independent of predetermined models limited to a number of cases, we automatically delineate a patient-specific aortic arch centerline by a series of Hough transforms, as done in [7], and then fit this centerline (instead of a predetermined model) to the likelihood image. The final shape of the aortic arch is then recovered by an inverse Euclidean distance transform.

Hough Circle Detection We first automatically delineate points along the centerline of the aortic arch by applying a series of circular Hough transforms. As the centerline of the aortic arch can roughly be described by a semicircle that is extended by two lines towards the inferior, we can easily restrict the Hough transformation space, once we know the radius of this semicircle. To estimate this

⁴ Note that basically almost any available method for automatic lung and airway tree extraction could be chosen, as we only need a very rough approximation of the lung area and the trachea, left, and right main bronchus.



(a) Definition of the first three search regions (in khaki) for circles representing the ascending, descending, and upper part of the aortic arch. (b) Hough circle extraction delineating the aortic arch.

Fig. 1: Hough circle extraction: (a) In two predefined search areas within the axial slice containing the carina and an oblique slice (khaki), we search for three initial Hough circles. (b) From the three centers of them another circle is computed (green). Along the upper semicircle and in the axial slices towards its inferior, we search for more Hough circles outlining the aortic arch.

radius, we search for two initial Hough circles (representing the ascending and descending aorta, respectively) inside the axial slice containing the carina and another Hough circle (representing the upper aortic arch) inside an oblique slice in between and orthogonal to the centers of the circles found in the axial slice (cf. Fig. 1a). During each Hough circle search, we restrict the search region to save computation time and avoid mis-detections. For the ascending aorta, we restrict this search region to the part of the axial slice containing the carina, which is enclosed by the mediastinal bounding box and to the anterior of the carina. For the descending aorta, we restrict it to the part enclosed by the mediastinal bounding box and to the posterior left of the carina. Once the first two circles and their centers are estimated, we can get a rough estimate of the radius of the aortic arch by computing the Euclidean distance between the two centers. We now search for a third circle in an oblique slice in between and orthogonal to the first two circle centers, which is centered the aortic arch radius away from the axial slice towards the superior. We set its size to five times the average radius of the first two circles.

During Hough circle extraction, the Hough map is computed only considering pixels between $t_{H_{\min}}$ and $t_{H_{\max}}$ in the input image, which is the typical edge intensity range of the aorta. For each pixel, we compute the Gaussian derivative of standard deviation σ_H to estimate the direction of the normal at that pixel. The Hough accumulator is filled by drawing lines between $r_{H_{\min}}$ and $r_{H_{\max}}$ (the typical minimum and maximum radii of the aorta) along the normal. We blur

the Hough map using a variance of v_H and compute the maxima in the Hough map. The highest maximum, which represents a full circle in our search area, is considered to belong to the aortic arch. The upper threshold $t_{H_{\max}}$ is automatically adjusted to the average intensity of the three initial circle centers to account for contrasted data, where the range of edge voxels is much larger.

When searching for the first three Hough circles, special care needs to be taken for the circle representing the ascending aorta, as the inferior vena cava and the brachiocephalic trunk (which both can appear circular) may be visible in the same axial slice. To select the correct circle, we apply a voting, which weights the corresponding value in the Hough map, the radius of the circle (as the ascending aorta is usually the largest of the three vessels), and the distance of the circle center to the carina along the mediolateral axis (as the ascending aorta in most cases is right above the carina):

$$a = \arg \max_{i=1\dots n} \left(\frac{h(\mathbf{x}_i)}{\max_{i=1\dots n} (h(\mathbf{x}_i))} \cdot \frac{r(\mathbf{x}_i)}{\max_{i=1\dots n} (r(\mathbf{x}_i))} \cdot \frac{d_{\text{car}_{\max}} - d_{\text{car}}(\mathbf{x}_i)}{d_{\text{car}_{\max}}} \right) \quad (1)$$

where $h(\mathbf{x}_i)$ is the value in the Hough map corresponding to circle i , $r(\mathbf{x}_i)$ is the radius of this circle, $d_{\text{car}}(\mathbf{x}_i)$ is the distance of the circle center to the carina in mediolateral direction, and $d_{\text{car}_{\max}}$ is half the mediastinal bounding box diameter in mediolateral direction. For the descending aorta, we just take the circle corresponding to the maximum value in the Hough map. For the upper aortic arch circle, we need to take care of the left pulmonary artery, which sometimes runs parallel below the upper aortic arch. Hence we perform another voting for the most probable circle:

$$u = \arg \max_{i=1\dots n} \left(\frac{h(\mathbf{x}_i)}{\max_{i=1\dots n} (h(\mathbf{x}_i))} \cdot \frac{r(\mathbf{x}_i)}{\max_{i=1\dots n} (r(\mathbf{x}_i))} \cdot \frac{d_{\text{cen}_{\max}} - d_{\text{cen}}(\mathbf{x}_i)}{d_{\text{cen}_{\max}}} \right) \quad (2)$$

where $d_{\text{cen}}(\mathbf{x}_i)$ is the Euclidean distance of the circle center to the slice center and $d_{\text{cen}_{\max}}$ is half the length of the diagonal of the oblique slice.

From the three center points of the Hough circles, we estimate a circle in 3D, its upper semicircle representing an estimate for the upper part of the aortic arch (cf. Fig. 1b).

Following the approach of [7], we reconstruct oblique 2-D slices of four times the size of the average radius of the three initial Hough circles in 15° steps along the semicircle. In each oblique slice, we search for the Hough circle with the maximum value in the corresponding Hough map. At each of the two ends of the semicircle, we start a search for the ascending and descending parts of the aortic arch. Every 12.5 mm we determine Hough circles in axial slices of the same size as before, iteratively adjusting the center of the current slice to the center coordinates of the previous Hough circle and adjusting the size of the 2-D slices to be four times the size of the average radius of the last three extracted circles (we hence take care for the facts that the aorta is not straight and the radius in the descending part is decreasing). We perform this process for the ascending aorta twice and for the descending aorta eight times. Overall, depending on the size of the data set, we get at most 23 initial centerline points.

NURBS Fitting From the initial centerline points, we generate a nonuniform rational B-spline (NURBS) curve that best fits the points in a least squares sense. We use 15 control points for the NURBS curve, so even if some of the centerline points are a little off, we get a good first approximation.

To match the curve with the real centerline of the aortic arch, we create a likelihood image of the centerline according to [12] (cf. Fig. 2a). In detail, we first perform a morphological opening using a sphere of size r_A on the median-filtered image to reduce variance of voxel intensities. Next, we detect edges in the opened image by computing the gradient magnitude and only leave voxels with a magnitude greater than t_{Δ_E} . As the variance of intensities inside blood vessels is usually low, we can reduce false edge candidates by computing the standard deviation at each edge candidate within a sphere of radius r_{σ_E} in the opened image and only leaving candidates whose standard deviation is greater than t_{σ_E} . Last, to generate the final likelihood image we apply a Euclidean distance transform to the edge image supplemented with "artificial" edge voxels obtained from all voxels of the rough lung segmentation. The likelihood image shows the distance between a voxel and its nearest edge voxel and thus the likelihood of a voxel to be part of the centerline. Using additional "artificial" edge voxels we ensure that all air voxels have zero likelihood to be part of the aorta.

In contrast enhanced data, the intensity distribution varies a lot within the contrasted region, leading to unwanted edges inside the aorta. To only consider its wall, we compute the average image intensity at the initial centerline points. If the average intensity exceeds a threshold t_C , we adjust all input voxels to be smaller or equal to t_C before performing above likelihood image generation steps.

Next, using the Powell optimizer, the NURBS curve is fitted to the likelihood image by minimizing following expression:

$$\arg \min_{\mathbf{P}_i} \left(-\frac{1}{m} \sum_{j=1}^m d_L^2 \left(N \left(\frac{j}{m} \right) \right) \right), \text{ where } N(u) = \sum_{i=1}^k R_{i,p} \mathbf{P}_i \quad (3)$$

Here, $d_L(\mathbf{X})$ is the Euclidean distance value of the voxel \mathbf{X} in the likelihood image, N is the NURBS curve, m is the number of sampling points along the curve (we sample every millimeter), $R_{i,p}$ are the rational basis functions of the curve (of degree $p = 3$ in our case), and $\mathbf{P}_i = (x_i, y_i, z_i)^T$ is the i th of k control points. Compared to [12] and [13], where one or more models need to be fitted globally as well as locally using several energy terms, we here greatly reduce the amount and complexity of optimizations to a single local minimization and energy term, making the approach faster and stable.

Finally, we recover the shape of the aortic arch by a reverse Euclidean distance transform, followed by a procedure to deal with false edges. In detail, we initialize each centerline voxel with the corresponding Euclidean distance from the likelihood image and draw a sphere of radius equal to this distance. As the likelihood image may still contain wrong edges, we grow each sphere iteratively, until the standard deviation of all voxels within the sphere exceeds t_{σ_R} . Each

iteration increases the radius of the sphere by the smallest of the three spatial resolutions of the input image.

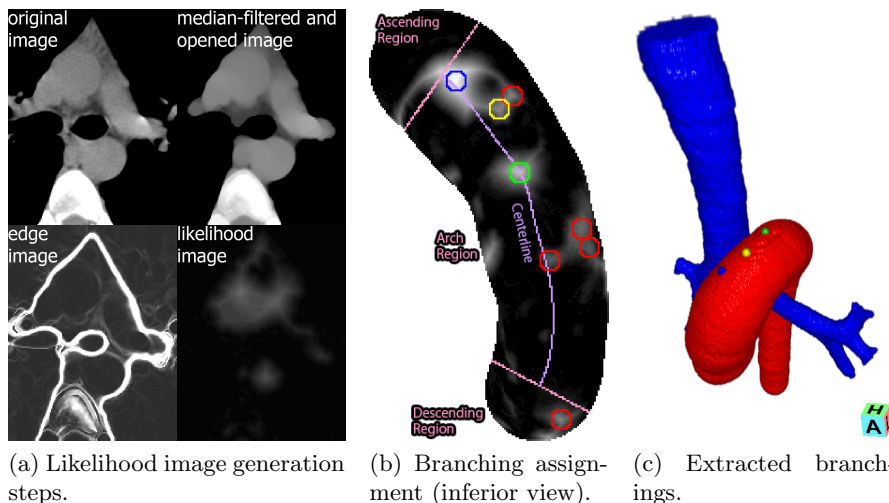


Fig. 2: Processing steps during branching assignment: (a) Generation of a 3-D likelihood image. (b) 2-D projection of the likelihood image and the centerline of the aortic arch segmentation (purple), and division of the projection into ascending, arch, and descending region by the pink lines. Each branching candidate is a local intensity maximum within a certain radius r_B represented by the colored circle. Red are unassigned candidates, blue are candidates assigned to the innominate artery, yellow to the left common carotid artery, and green to the left subclavian artery. (c) Final branching assignment results.

2.3 Branching Extraction

The extraction of all branchings is motivated by the fact that the innominate, left common carotid, and left subclavian arteries branch off the aortic arch in superior direction. We incorporate three properties of the branchings into our algorithm. First, we search for voxels along the boundary of the aortic arch, which have a higher local Euclidean distance (likelihood) than others. Second, the closer the voxels are to the upper ridge of the aortic arch, the more likely they are branchings. And third, the branching arteries usually have a certain distance to each other.

Preprocessing Before starting our branching extraction, we preprocess the input image in the same way as for aortic arch segmentation to obtain a likelihood image (cf. Fig. 2a), including thresholding with t_C in case of contrast enhanced data. However, as the average diameter of the aortic arch branches is smaller

than that of the arch itself, we reduce the radius of the structuring element for morphological opening to r_B in order not to "smooth away" small branches.

Parallel Projection After preprocessing, we create the (one-voxel thick) boundary of the upper aortic arch segmentation. To simplify our branching search, we reduce the search space from three to two dimensions: starting from the axial slice containing the carina, we perform a parallel projection of the likelihood voxels inside the boundary onto a single image, in the following referred to as 2-D likelihood image. Furthermore, for the 2-D likelihood image, we compute the 2-D Euclidean distance transform to its boundary. This image, in the following referred to as 2-D boundary distance image, is an indicator for the likelihood of a candidate to be a branching, as the upper ridge of the aortic arch roughly corresponds to high values in the 2-D boundary distance image.

At the same time we perform a parallel projection of the segmented centerline of the aortic arch and approximate a 2-D NURBS curve n to this centerline projection, which again roughly overlaps with the upper ridge of the arch. For each point \mathbf{x} in the 2-D likelihood image or the 2-D boundary distance image, we define its offset $\delta(\mathbf{x})$ to the first control point of n along the curve by

$$\delta(\mathbf{x}) = \begin{cases} -|n(0) - \mathbf{x}| & \text{if } f(\mathbf{x}) = 0 & \text{(ascending region)} \\ l_n(0, f(\mathbf{x})) & \text{if } 0 < f(\mathbf{x}) < 1 & \text{(arch region)} \\ l_n(0, 1) + |n(1) - \mathbf{x}| & \text{if } f(\mathbf{x}) = 1 & \text{(descending region)} \end{cases} \quad (4)$$

where $l_n(a, b)$ gives the arc length along n between a and b and $f(\mathbf{x})$ gives the parameter of the point on the curve closest to \mathbf{x} . Using $\delta(\mathbf{x})$, we can also assign one of three approximate regions (ascending, arch, descending) to each point (cf. Fig. 2b).

Branching Assignment In the 2-D likelihood image, we search for local maxima greater than r_B within a radius of r_B , whose neighbors within r_B are all inside the boundary of the 2-D likelihood image. These maxima represent our initial branching candidates, which we now need to identify the correct ones from and assign correct arteries to.

Innominate Artery As the innominate artery branching may be located at many possible positions along the upper aortic arch and the innominate and left subclavian artery may have very similar radii and thus likelihoods, we cannot simply select the innominate as the candidate with the highest likelihood. We first need to restrict our search area along the upper aortic arch. Therefore, we compute the average weighted distance d_w of all candidates to the first control point of n by

$$d_w = \frac{\sum_{j=1}^w \delta(\mathbf{x}_j) \cdot d_1(\mathbf{x}_j)}{\sum_{j=1}^w d_1(\mathbf{x}_j)} \quad (5)$$

where $d_1(\mathbf{x})$ is the Euclidean distance value of the pixel \mathbf{x} in the likelihood image. The candidate positioned below d_w (i.e. towards the ascending region) with the highest likelihood is assigned to the innominate artery.

However, the innominate artery is often adjacent to the left innominate vein, so sometimes no distinct border between them is visible, which can lead to several local likelihood maxima. Therefore, if it is located in the ascending region along with other candidates, we update the index i of the most probable candidate to

$$i = \arg \max_{j=1\dots w} \left(\frac{d_1(\mathbf{x}_j)}{\max_{j=1\dots w} (d_1(\mathbf{x}_j))} \cdot \frac{d_b(\mathbf{x}_j)}{d_b(n(0))} \right) \quad (6)$$

where $d_b(\mathbf{x})$ is the value of the pixel \mathbf{x} in the boundary distance image and w is the number of candidates. This favors posterior candidates with higher likelihood.

Left Subclavian Artery As we got some of the branching candidates due to merges of the aortic arch with adjacent tissue, and the thickness of the left subclavian and left common carotid arteries can be similar and much smaller than that of the innominate artery, we cannot simply search for the second largest value in the 2-D likelihood image. We need to consider their natural positions relative to each other.

So first we compute the offset $d_i(\mathbf{x}_j) = \delta(\mathbf{x}_j) - \delta(\mathbf{x}_i)$ between the remaining candidates and the branching of the innominate artery. If the remaining candidates lie posterior to the innominate artery branching and are at most the arc length $l_n(0, 1)$ of the whole centerline curve away, we further consider them in the following expression to get the index s of the most likely candidate for the left subclavian artery:

$$s = \arg \max_{j=1\dots v} \left(\frac{d_1(\mathbf{x}_j)}{\max_{j=1\dots v} (d_1(\mathbf{x}_j))} \cdot \frac{d_b(\mathbf{x}_j)}{d_b(n(f(\mathbf{x}_j)))} \cdot \left(1 - \frac{|l_n(0, \frac{1}{3}) - d_i(\mathbf{x}_j)|}{l_n(0, \frac{2}{3})} \right) \right) \quad (7)$$

Here we account for the facts that the likelihood should be as high as possible, the candidate should be as close to the centerline as possible, and the branching of the left subclavian artery should be about one third the arc length of the centerline curve away from the branching of the innominate artery.

Left Common Carotid Artery All u remaining candidates are considered in a final step, if they lie in between the innominate and left subclavian artery (i.e. $0 < d_i(\mathbf{x}_j)$ and $0 < d_s(\mathbf{x}_j) = \delta(\mathbf{x}_s) - \delta(\mathbf{x}_j)$), are approximately on a line connecting the innominate and left subclavian artery (i.e. the angle between this line and the line connecting the candidate and the left subclavian artery should not get too big, in our case less than 40 degrees), and are superior to the inferior of the two (looking at their original depth in 3D). From the indexes of these candidates, we choose the most likely one c for the left common carotid artery by

$$c = \arg \max_{j=1\dots u} \left(\frac{d_1(\mathbf{x}_j)}{\max_{j=1\dots u} (d_1(\mathbf{x}_j))} \cdot \frac{d_b(\mathbf{x}_j)}{d_b(n(f(\mathbf{x}_j)))} \cdot \left(1 - \frac{|d_s(\mathbf{x}_j) - d_i(\mathbf{x}_j)|}{d_s(\mathbf{x}_j) + d_i(\mathbf{x}_j)} \right) \right) \quad (8)$$

Here we favor candidates, which lie half way between the branchings of the innominate and the left subclavian artery.

3 Results

We evaluated our method on 10 contrast enhanced and 30 non-contrast chest CT data sets of various hospitals, scanners, and acquisition parameters. The 40 data sets consisted of 99 – 838 slices spaced 0.4 – 1.5 mm. Each axial slice had 512×512 pixels of size 0.5 – 0.665 mm. For each data set, we manually segmented the aortic arch and extracted its branchings, which took approximately one to two hours per data set. For the automatic algorithm, we used the parameters shown in Table 1.

Table 1: Values of parameters used for evaluation (HU refers to Hounsfield units).

s_m : $3 \times 3 \times 3$ voxels	$t_{H_{\min}}$: -60 HU	v_H : 5 pixels	t_{Δ_E} : 10 HU
t_C : 200 HU	$t_{H_{\max}}$: 40 HU	σ_H : 5 pixels	r_{σ_E} : 3 voxels
r_A : 4 mm	$r_{H_{\min}}$: 7 mm		t_{σ_E} : 15 HU
r_B : 2.5 mm	$r_{H_{\max}}$: 28 mm		t_{σ_R} : 8 HU

For each data set, we computed the sensitivity, specificity, and Jaccard index between the manually and automatically segmented 3-D volumes (considering voxels within the bounding box of the two segmentations only) and their mean, standard deviation (SD), and minimum. We also computed the mean, SD, and maximum of the minimum Euclidean distances (MD) of the contours of the two segmentations and their mean, SD, and maximum. Furthermore, we counted the number of false positives (i.e. branchings outside their corresponding artery) and false negatives (i.e. missed branchings) for all 40 data sets and computed the mean, standard deviation, and maximum of the Euclidean distances between all manually and automatically selected branchings. Finally, on a workstation with two 64-bit Quad-Core Intel Xeon 5355 processors and 16 GB main memory we measured the runtime of our automatic method, separated into preprocessing, aorta, branching extraction, and total runtime, along with their mean, SD, and maximum. Table 2 summarizes all results.

Table 2: Results of our evaluation.

Aortic Arch Segmentation							
Sensitivity	Specificity	Jaccard Index	Mean MD (mm)	SD MD (mm)	Max MD (mm)		
$0.95 \pm 0.03 \geq 0.89$	$0.99 \pm 0.00 \geq 0.98$	$0.92 \pm 0.02 \geq 0.85$	$0.4 \pm 0.1 \leq 0.9$	$0.5 \pm 0.1 \leq 0.9$	$3.6 \pm 1.2 \leq 6.9$		
Branching Extraction			Runtime (s)				
Distance (mm)	TP	FP	FN	Preprocessing	Aortic Arch	Branching	Total
$2.0 \pm 1.1 \leq 6.1$	114	0	3	$68 \pm 23 \leq 106$	$74 \pm 42 \leq 179$	$12 \pm 5 \leq 21$	$154 \pm 65 \leq 298$

4 Discussion

Our results show that, at an acceptable average total runtime of about 2.5 minutes and a mean distance of less than half a millimeter between manual and automatic segmentation, the aortic arch could be extracted well. As can be seen in Table 3, we also improve the state of the art in aortic arch segmentation.

As already mentioned in [12, 13], problems can arise when cardiac motion or calcifications induce imaging artifacts and when the pulmonary artery, superior

Table 3: Comparison of our method to the state of the art in automatic aortic arch extraction. In [13], results were not assessed quantitatively. Due to global and local fitting to one or several models, [12] and [13] are expected to have a longer runtime than our method.

Method	Non-/Contrast	Successful/Cases	Mean MD (mm)	Runtime (min)
Kovács et al. [7]	No/Yes	17/21	1.1±0.2	~6
Peters et al. [9]	No/Yes	36/37	0.6±1.1	0.2
Kitasaka et al. [12]	Yes/No	7/7	0.5±0.2	NA
Taeprasartsit & Higgins [13]	Yes/Yes	12/13	NA	NA
Ours	Yes/Yes	40/40	0.4±0.1	~2.5

vena cava, or other tissue is adjacent to the aorta, leading to slight overlaps and mis-extractions. However, our quantitative analysis (cf. Table 2) shows that all mis-extractions are minor and do not influence the performance of our branching extraction significantly.

The mean distance between manually and automatically extracted branchings was 2 millimeters. Only 3 out of 117 branchings could not be found by our algorithm. Similar to aortic arch extraction, this usually happened when the left common carotid artery was too close to one of the others and in the presence of calcifications or imaging artifacts, so no distinct local likelihood maximum could be found.

In 3 of our 40 cases, the common carotid artery was branching off the innominate artery instead of the aortic arch. Our method handled all these cases correctly by only assigning two branchings. In about 4.6% of a larger study [2], four arteries branched off the aortic arch. As none of our 40 evaluation cases covered such a branching pattern, we need to further analyze the common location of the fourth artery and integrate it into our method, e.g. by utilizing pattern classification techniques.

5 Conclusion

We developed a new method for the automatic detection of the main arterial branchings of the aortic arch, based on a robust technique for automatic aortic arch extraction in chest CT that extends and improves the current state of the art [7,12,13]. Our method works stable on both contrast enhanced and non-contrast CT, making it applicable to a large number of data sets. It can support the physician’s diagnosis and treatment planning and provides valuable landmarks for further segmentation of the aortic branches, intra- and interpatient registration of the mediastinum, or chest atlas generation.

Acknowledgments

Parts of this research were supported by the Japan Society for the Promotion of Science (JSPS) postdoctoral fellowship program for foreign researchers, a Grant-In-Aid for Scientific Research from JSPS, the program of formation of innovation center for fusion of advanced technologies ”Establishment of early

preventing medical treatment based on medical-engineering for analysis and diagnosis” funded by the Ministry of Education (MEXT), and a Grant-In-Aid for Cancer Research from the Ministry of Health, Labour and Welfare.

References

1. Taeprasartsit, P., Higgins, W.E.: System for definition of the central-chest vasculature. In: SPIE Medical Imaging. (2009)
2. Nelson, M.L., Sparks, C.D.: Unusual aortic arch variation: Distal origin of common carotid arteries. *Clinical Anatomy* **14** (2001) 62–65
3. Subramanyan, K., Steinmiller, M., Sifri, D., Boll, D.: Automatic aortic vessel tree extraction and thrombus detection in multislice CT. In: SPIE Medical Imaging. (2003)
4. de Bruijne, M., van Ginneken, B., Viergever, M.A., Niessen, W.J.: Interactive segmentation of abdominal aortic aneurysms in CTA images. *Medical Image Analysis* **8**(2) (2003) 127–138
5. Olabarriaga, S.D., Rouet, J.M., Fradkin, M., Breeuwer, M., Niessen, W.J.: Segmentation of thrombus in abdominal aortic aneurysms from CTA with nonparametric statistical grey level appearance modeling. *IEEE Transactions on Medical Imaging* **24**(4) (2005) 477–485
6. Behrens, T., Rohr, K., Stiehl, H.S.: Robust segmentation of tubular structures in 3-D medical images by parametric object detection and tracking. *IEEE Trans Syst Man Cybern B Cybern.* **33**(4) (2003) 554–561
7. Kovács, T., Cattin, P., Alkadhi, H., Wildermuth, S., Székely, G.: Automatic segmentation of the vessel lumen from 3D CTA images of aortic dissection. In: *Bildverarbeitung für die Medizin*. (2006)
8. O’Donnell, T., Gupta, A., Boulton, T.: A new model for the recovery of cylindrical structures from medical image data. In: *CVRMed-MRCAS*. (1997)
9. Peters, J., Ecabert, O., Lorenz, C., von Berg, J., Walker, M.J., Ivanc, T.B., Vembar, M., Olszewski, M.E., Weese, J.: Segmentation of the heart and major vascular structures in cardiovascular CT images. In: SPIE Medical Imaging. (2008)
10. Išgum, I., Rutten, A., Prokop, M., van Ginneken, B.: Detection of coronary calcifications from computed tomography scans for automated risk assessment of coronary artery disease. *Medical Physics* **34**(4) (2007) 1450–1461
11. Kurkure, U., Avila-Montes, O., Kakadiaris, I.: Automated segmentation of thoracic aorta in non-contrast CT images. In: *ISBI*. (2008)
12. Kitasaka, T., Mori, K., Hasegawa, J., Toriwaki, J., Katada, K.: Automated extraction of aorta and pulmonary artery in mediastinum from 3D chest X-ray CT images without contrast medium. In: SPIE Medical Imaging. (2002)
13. Taeprasartsit, P., Higgins, W.E.: Method for extracting the aorta from 3D CT images. In: SPIE Medical Imaging. (2007)
14. Kunz, P., Scholz, M., Haas, B., Coradi, T.: Anatomic orientation in medical images (2008)
15. Hu, S., Hoffman, E.A., Reinhardt, J.M.: Automatic lung segmentation for accurate quantitation of volumetric X-ray CT images. *IEEE Transactions on Medical Imaging* **20**(6) (2001) 490–498
16. Kitasaka, T., Mori, K., Suenaga, Y., Hasegawa, J., Toriwaki, J.: A method for segmenting bronchial trees from 3D chest X-ray CT images. In: *MICCAI*. (2003)